# Dark discrete breather modes in a monoaxial chiral helimagnet with easy-plane anisotropy

I. G. Bostrem,[1] E. G. Ekomasov,[2,3] J. Kishine,[4,5] A. S. Ovchinnikov,[1,6] and Vl. E. Sinitsyn[1]
[1]*Institute of Natural Science and Mathematics, Ural Federal University, Ekaterinburg 620002, Russia*
[2]*Bashkir State University, Institute of Physics and Technology, Ufa 450076, Russia*
[3]*Tyumen State University, Institute of Physics and Technology, Tyumen 625003, Russia*
[4]*Division of Natural and Environmental Sciences, The Open University of Japan, Chiba 261-8586, Japan*
[5]*Institute for Molecular Science, 38 Nishigo-Naka, Myodaiji, Okazaki 444-8585, Japan*
[6]*Institute of Metal Physics, Ural Division, Russian Academy of Sciences, Ekaterinburg 620219, Russia*

(Received 4 September 2021; revised 6 November 2021; accepted 3 December 2021; published 15 December 2021; corrected 28 November 2022)

Nonlinearity and discreteness are two pivotal factors for an emergence of discrete breather excitations in various media. We argue that these requirements are met in the forced ferromagnetic phase of the monoaxial chiral helimagnet $CrNb_3S_6$ due to the specific domain structure of the compound. The stationary, time-periodic breather modes appear as the discrete breather lattice solutions whose period mismatches with a system size. Thanks to easy-plane single-ion anisotropy intrinsic to $CrNb_3S_6$, these modes are of the dark type with frequencies lying within the linear spin-wave band, close to its bottom edge. They represent cnoidal states of magnetization, similar to the well-known soliton lattice ground state, with differing but limited number of embedded $2\pi$ kinks. The linear stability of these dark breather modes is verified by means of Floquet analysis. Their energy, which is controlled by two parameters, namely, the breather lattice period and amplitude, falls off linearly with a growth of the kink number. These results may pave a path to design spintronic resonators on the base of chiral helimagnets.

DOI: 10.1103/PhysRevB.104.214420

## I. INTRODUCTION

Nonlinear magnetic phenomena, where solitonlike waves are involved, have been extensively discussed for many decades, and a wealth of information has been accumulated on the subject since that time [1]. Among various nonlinear coherent structures, such as kinks, vortices, or monopoles, breathers may appear as generic solutions of nonlinear dynamics in a wide range of physical systems [2]. Unlike other solitonlike solutions, which preserve their shape as they propagate, the breathers are characterized by spatial localization and periodic oscillations in time. This localization is realized in perfectly regular systems as opposed to disorder-induced Anderson localization.

When considering the discrete aspects of nonlinear lattice problems, the modified concept of discrete breathers (DB) is introduced [3–5]. Discreteness is essential to preventing resonances between the breather modes and the system characteristic frequencies. Contrary to continuous solitons, DBs do not require integrability for their existence and stability. They are not confined to a specific spatial dimension and have an amplitude-dependent frequency. The DB basic properties must be complemented by their division into the stationary and moving modes [6]. These nonlinear excitations have been observed in a variety of physical systems, where discreteness arises either as an intrinsic property of the underlying lattice, such as lattice dynamics of halide-bridged transition metal complexes [7] and PbSe crystal [8], layered crystal insulator [9], or in artificially designed arrays of coupled Josephson junctions [10,11], coupled pendula [12], micromechanical cantilevers [13], optical waveguides [14], in compressed diatomic granular one-dimensional (1D) crystal [15], and in electrical circuits with series-connected tunnel diodes [16].

As for DB excitations in spin lattices, they have been predicted for antiferromagnetic chains [17] with subsequent direct experimental verification [18,19]. Currently, considerable numerical and theoretical progress has been achieved in understanding the nature of DB in Heisenberg spin chains with additional interactions, for instance, onsite anisotropy or next-nearest-neighbor exchange interactions [20–26]. Recently, formation of discrete breathers has been analyzed for weak ferromagnetic chains where the presence of the Dzyaloshinskii-Moriya (DM) interaction leads to a small canting between the interacting moments [27,28]. The DB solutions have been examined in the dynamics of the 1D array of magnetic particles (dots) with easy-plane anisotropy and interparticle magnetic dipole interaction [29].

Most realistic discrete systems may be reformulated for appropriate continuous media that often provide an adequate description of nonlinear properties, and, in some cases, analytical expressions in closed form may be derived [1,30–33]. However, it is quite possible that some nonlinear phenomena in continuous models cannot appear in their discrete counterparts, and more comprehensive treatment is required to gain a deeper insight into the problem [34,35]. One such issue is whether the discrete system supports breather lattice (BL) solutions, which represent a regularly ordered array of single breathers. These periodic solutions may be expressed in terms of Jacobi elliptic functions [36] and occur naturally for the continuous nonlinear equations, such as the sine-Gordon equation [37–39], sinh-Gordon equation [40], Korteweg–de Vries (KdV) equation [41], modified KdV equa-

 

tion [42–44], and the nonlinear Schrödinger equation [45]. Applications of the periodic breather modes to various continuous media have been discussed in Refs. [46–49]. The BL solution has been predicted for a continuous $\beta$-Fermi-Pasta-Ulam (FPU) chain [50], finding periodic DB configurations in a triangular $\beta$-FPU lattice has been recently reported [51]. As for discrete spin lattices, spatially periodic breather-type solutions have been traced numerically in pioneering work [52], where they were named intrinsic localized spin modes of dark types by analogy with the optic solitons [53,54]. However, to our knowledge their analytical expressions are still lacking.

In this paper we argue that the phase of forced ferromagnetism in the monoaxial chiral helimagnet $CrNb_3S_6$ assumes the existence of BL excitations. These modes are intrinsically stationary due to the specific domain structure of $CrNb_3S_6$ samples composed of 1-$\mu$m-wide grains with different, left- or right-hand, crystallographic structural chirality [55]. We demonstrate analytically and numerically that these spatially periodic standing solutions with amplitude varying in time may be categorized into four types, depending on the position of their frequencies with respect to the spectrum of linear spin waves. This position is set by a value and sign of single-ion anisotropy, and, as a consequence, the only type of BL solutions that is allowed by fairly small easy-plane anisotropy in $CrNb_3S_6$ is the so-called dark breather modes emerging within the spin-wave band, close to its bottom edge. They represent cnoidal states of magnetization, similar to the soliton lattice ground state, with different numbers of embedded kinks. The salient features of the "bottom dark" breather lattice are its period incommensurate with a system size and its energy falling off linearly with the growth of a number of kinks. The linear stability of these modes is verified by means of Floquet analysis.

It should be emphasized at the outset that previous theoretical investigations of DB modes in ferromagnetic chains with on-site anisotropies [20,21,52] were inspired by experimental studies of spin dynamics in the linear chain compound $CsFeCl_3$ [56], for which intrinsic single-ion anisotropy exceeds intersite exchange coupling. A similar situation was dealt in Ref. [29], where magnetic dots with a strong easy-plane anisotropy are coupled by weak magnetic dipole interaction. In contrast, our treatment is targeted at search of DB solutions for the case when exchange coupling between the nearest moments is much larger than on-site magnetic anisotropy.

The paper is organized as follows. In Sec. II we describe a model and give classification of periodic breather solutions. In Sec. III we present results of numerical simulation of breather lattices based on discrete equations of spin motion. In Sec. IV we present a detailed analysis of dark breather modes emerging near the bottom edge of the spin-wave spectrum. The conclusions and discussions are given in Sec. V.

## II. MODEL

The model Hamiltonian of the chiral monoaxial helimagnet is of the form

$$\mathcal{H} = -2J\sum_n \mathbf{S}_n\cdot\mathbf{S}_{n+1} + A\sum_n \left(S_n^z\right)^2 + D\sum_n [\mathbf{S}_n\times\mathbf{S}_{n+1}]_z - H\sum_n S_n^z, \quad (1)$$

where the first term is the exchange coupling along the chiral axis ($z$ axis) with $J>0$. The second describes the single-ion anisotropy with the constant $A$, while the third describes the Dzyaloshinskii-Moriya interaction of strength $D$. The last term denotes Zeeman coupling with an external magnetic field $H$ directed along the $z$ axis. The magnetic field is assumed to be strong enough so that in the ground state all spins are ordered along the external field direction. This forced ferromagnetic arrangement requires $H > 2S(\sqrt{4J^2+D^2}-J+A)$ [57].

The appropriate spin variables $s_n^{\pm} = (S_n^x \pm iS_n^y)/S$ and $s_n^z = S_n^z/S$ describe spin deviations from the ground state, where $S$ is the magnitude of spin.

The equations of motion for these variables become

$$\frac{i\hbar}{2JS}\frac{d}{dt}s_n^+ = s_n^+\left(s_{n+1}^z + s_{n-1}^z\right) - s_n^z(s_{n-1}^+ + s_{n+1}^+) - 2Bs_n^+ s_n^z + i\frac{D}{2J}s_n^z(s_{n-1}^+ - s_{n+1}^+) + \frac{H}{2JS}s_n^+, \quad (2)$$

where $s_n^z = \sqrt{1-|s_n^+|^2}$ and $B = A/2J$.

Time-dependent solutions $s_n^+ = s_n(t)\exp(ikna - i\omega t)$ with wave number $k$ and frequency $\omega$ can be found, where the amplitude $s_n$ is called *the transverse spin accumulation* and $a$ being the lattice constant. Substituting this form into Eq. (2) and collecting separately real and imaginary parts we obtain the system

$$\Omega s_n = s_n\left(\sqrt{1-s_{n+1}^2}+\sqrt{1-s_{n-1}^2}\right) - 2Bs_n\sqrt{1-s_n^2} - \sqrt{1-s_n^2}(s_{n-1}+s_{n+1})\sqrt{1+\frac{D^2}{4J^2}}\cos(ka+\delta), \quad (3)$$

$$\frac{ds_n}{d\tau} = \sqrt{1-s_n^2}(s_{n-1}-s_{n+1})\sqrt{1+\frac{D^2}{4J^2}}\sin(ka+\delta), \quad (4)$$

where $\tau = t/t_0$ is the dimensionless time with $t_0 = \hbar/(2JS)$, the effective frequency $\Omega = (\hbar\omega - H)/2JS$, and the phase shift is determined from $\delta = \tan^{-1}(D/2J)$.

Breather spin modes are expected to exist in perfect discrete magnetic chains due to salient nonlinearity in the exchange and anisotropy interactions. These modes may lie inside the linear wave band and split off from its upper or lower edges, so-called DB solutions of the dark type [52]. By contrast, the bright-type modes can appear at frequencies either just above the upper band edge or just below the lower edge of the linear spin-wave spectrum.

In the small spin deviation limit, the linear dispersion curve for the spin wave is obtained from Eq. (3) as

$$\Omega(k) = 2 - 2B - 2\sqrt{1+\frac{D^2}{4J^2}}\cos ka. \quad (5)$$

The top and bottom zone boundaries of the plane-wave spectrum take the values $\Omega(\pi) = 2-2B+2\sqrt{1+\frac{D^2}{4J^2}}$ and $\Omega(0) = 2-2B-2\sqrt{1+\frac{D^2}{4J^2}}$, respectively.

Concerning the DB wave number, it coincides with that of the simple or conical spirals in the static case when $ds_n/d\tau = 0$, i.e., $ka = -\tan^{-1}(D/2J)$. It immediately follows from Eq. (3).

To start with we focus on the upper band edge and consider both bright and dark excitations. As the orientational order of transversal spin components in these breather modes is close to that of the corresponding linear spin waves, i.e., to the antiferromagnetic one, it is convenient to introduce the envelope function $\psi(z) = (-1)^n s_n$, where $z = na$, which varies slowly in space.

As will be seen in the next section, the DB lattice modes may be compared with periodic solutions of the nonlinear Duffing equation [21,47],

$$\frac{d^2\psi}{d\tilde{z}^2} - \alpha\psi + \beta\psi^3 = 0, \tag{6}$$

which can be deduced from Eq. (3) if keeping only the leading cubic nonlinearity (for details, see Appendix). Here, $\tilde{z} = z/a$ is the dimensionless coordinate expressed in lattice units, and

$$\alpha = \frac{\Omega - \Omega(\pi)}{\sqrt{1 + \frac{D^2}{4J^2}}}, \quad \beta = -\frac{\Omega(\pi)}{2\sqrt{1 + \frac{D^2}{4J^2}}}. \tag{7}$$

For the case $\alpha > 0$, $\beta > 0$ the *bright* BL solution centered at $\tilde{z}_0$ is obtained as

$$\psi_b^{(+)}(\tilde{z}) = \left[\sqrt{\frac{2c}{\beta} + \frac{\alpha^2}{\beta^2}} + \frac{\alpha}{\beta}\right]^{\frac{1}{2}} \mathrm{cn}\left[\frac{4K}{L_b^{(+)}}(\tilde{z} - \tilde{z}_0), \kappa^2\right], \tag{8}$$

where cn(. . .) is the Jacobi elliptic function with the modulus

$$\kappa^2 = \frac{1}{2}\frac{\alpha + \sqrt{\alpha^2 + 2\beta c}}{\sqrt{\alpha^2 + 2\beta c}}. \tag{9}$$

The constant $c$ can take only positive values for these solutions that the superscript "+" refers to. Together with the requirement of smallness of $\psi_b^{(+)}$, it results in the condition

$$0 < c < \frac{\beta}{2} - \alpha. \tag{10}$$

The constant $c$ specifies the amplitude and the bright BL period $L_b^{(+)} = 4K(\alpha^2 + 2\beta c)^{-\frac{1}{4}}$, where $K$ is the elliptic integral of the first kind. For a finite-size system $c$ may be derived from the requirement that dynamics of the edge and interior spins must be consistent (see Sec. III for details).

In the opposite case $c < 0$, the solution is given by

$$\psi_b^{(-)}(\tilde{z}) = \left[\frac{\alpha}{\beta} - \sqrt{\frac{2c}{\beta} + \frac{\alpha^2}{\beta^2}}\right]^{\frac{1}{2}} \mathrm{nd}\left[\frac{2K}{L_b^{(-)}}(\tilde{z} - \tilde{z}_0), \kappa^2\right], \tag{11}$$

where nd(. . .) is the Jacobi elliptic function $\mathrm{dn}^{-1}(\ldots)$ with the modulus

$$\kappa^2 = \frac{2\sqrt{\frac{\alpha^2}{\beta^2} + \frac{2c}{\beta}}}{\frac{\alpha}{\beta} + \sqrt{\frac{\alpha^2}{\beta^2} + \frac{2c}{\beta}}}, \tag{12}$$

and the period $L_b^{(-)} = \sqrt{8}K[\alpha + \sqrt{\alpha^2 + 2\beta c}]^{-\frac{1}{2}}$. In contrast to (10), the $c$ values are bounded from below $c > -\alpha^2/(2\beta^2)$.

As expected, in the limit $\kappa^2 = 1$, when $c = 0$, the bright breather lattice (8) reduces to the single breather solution

$$\psi_b(\tilde{z}) = \sqrt{\frac{2\alpha}{\beta}}\frac{1}{\cosh[\sqrt{\alpha}(\tilde{z} - \tilde{z}_0)]} \tag{13}$$

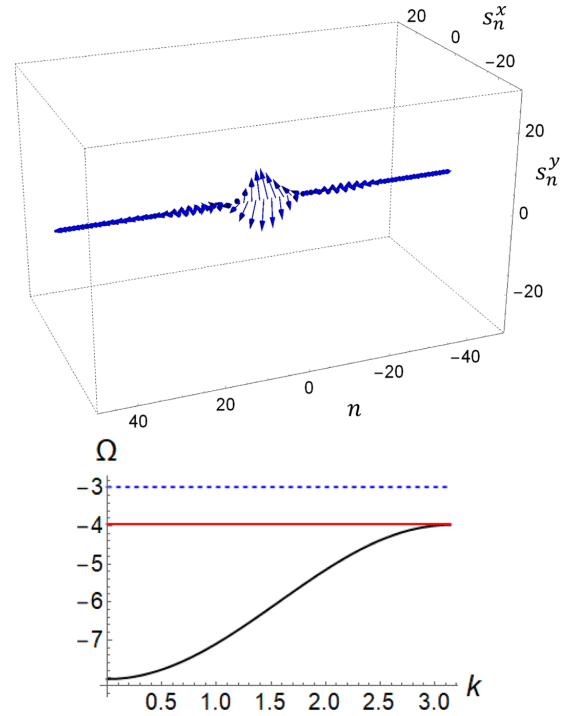


FIG. 1. The top bright breather mode with one kink-antikink bound pair in the envelope function built from numerical simulations (upper panel). Transversal spin components (relative to the chain axis) are shown with a factor 50 expansion. Lower panel: The spin-wave spectrum at $B = 4.0$ (black solid). The breather frequency $\Omega = -3.95$ (red solid) is limited from above by $\Omega_u = \frac{3}{2}[1 - B + \sqrt{1 + (D/2J)^2}]$ (blue dashed).

with a peak shape of width $1/\sqrt{\alpha}$ centered around $\tilde{z}_0$, which can be loosely be thought of as a "bound state" of a kink and antikink. In contrast, the solution (11) approaches zero when $\kappa^2$ goes to 1, but for all other $\kappa$ values the classification based on the number of kink-antikink bound pairs may be retained.

The numerical solution corresponding to the bright BL mode with the envelope function (8) is presented in Fig. 1 (for details, see Sec. III). It is known that the existence of such intrinsic localized modes (ILSMs) for a ferromagnetic chain with nearest-neighbor interactions requires that the strength of the single-ion anisotropy exceeds a certain critical value so that the resulting ILSM frequencies can appear above the linear spin-wave band [17]. In our case, the requirement $\beta > 0$ imposes the restriction on the allowed anisotropy strength, $B > 1 + \sqrt{1 + D^2/4J^2}$, whereby it must exceed the Heisenberg exchange coupling. The condition is not suitable for the chiral helimagnet $CrNb_3S_6$, where $B \sim 0.15$ [58] is close to the value for the antisymmetric exchange $D/2J \sim 0.16$ [59]. Notwithstanding, there are nonchiral magnetic materials, such as $CsFeCl_3$ or some quasi-1D metal-organic compounds, where this somewhat exotic situation takes place [60].

The opposite situation, $\alpha < 0$ and $\beta < 0$, leads to the lattice breather solution of the *dark* type:

$$\psi_d^{(+)}(\tilde{z}) = \pm\sqrt{\frac{\alpha}{\beta} - \sqrt{\frac{\alpha^2}{\beta^2} + \frac{2c}{\beta}}}\,\mathrm{sn}\left[\frac{4K}{L_d}(\tilde{z} - \tilde{z}_0), \kappa^2\right], \tag{14}$$

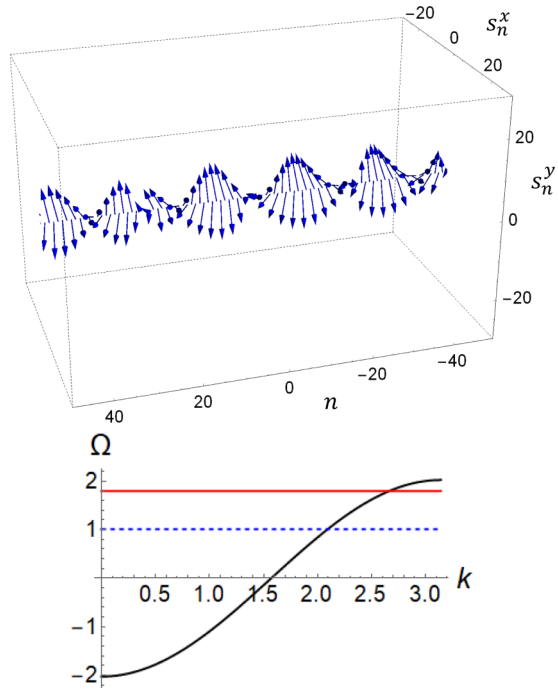


FIG. 2. The top dark breather mode with four successive kink/antikinks in the envelope function built from numerical simulations (upper panel). Transversal spin components (relative to the chain axis) are shown with a factor 20 expansion. Lower panel: Dispersion of the linear spin waves at the easy-plane anisotropy $B = 1.0$ (solid black). The breather frequency $\Omega = 1.8$ is limited by the top edge of the spin-wave spectrum and $\Omega_d = 1 - B + \sqrt{1 + (D/2J)^2}$ (blue dashed).

with the elliptic modulus

$$\kappa^2 = \frac{\alpha + \sqrt{\alpha^2 + 2\beta c}}{\alpha - \sqrt{\alpha^2 + 2\beta c}} \tag{15}$$

and the period $L_d = 4K(-\alpha/2 + \sqrt{\alpha^2/4 + \beta c/2})^{-\frac{1}{2}}$. The condition on the parameter $c$, which is positive, repeats that of the bright modes (10). Note that at $c < 0$ only unbounded solutions appear what makes them inappropriate as finite-amplitude excitations.

The corresponding single breather solution is retrieved when $\kappa^2 \to 1$, or $c \to -\alpha^2/(2\beta)$,

$$\psi_d(\tilde{z}) = \pm\sqrt{\frac{\alpha}{\beta}}\tanh\left[\sqrt{-\frac{\alpha}{2}}(\tilde{z} - \tilde{z}_0)\right]. \tag{16}$$

It describes a kink whose inverse width is $\sqrt{|\alpha|/2}$. Based on the form (16), breather lattices of the dark type may be categorized according to the number of consecutively embedded S-shaped kinks/antikinks.

An example of the dark-type DB excitations found numerically is shown in Fig. 2. Its envelope function fits well with the expression (14) (see Sec. III for details). Here we just note that the derivation of the dark breather solution is based on the assumption $\alpha < 0$, thereby meaning that the effective frequency of the localized mode cannot be above the top of the spin-wave spectrum, $\Omega < \Omega(\pi)$ [see Eq. (7)]. Similarly to the case of bright modes, this fact results from the restriction on the single-ion anisotropy constant, $B < 1 + \sqrt{1 + D^2/4J^2}$, originated formally from $\beta < 0$. Although this estimate allows the *top dark* BL solutions (14) for fairly small easy-plane anisotropy valid for $CrNb_3S_6$, the requirement $B > 0$ turns out to be incompatible with a smooth spin arrangement at the boundaries (see Sec. III).

We now turn to the lower edge of the spin-wave band, where bright and dark DB modes may be also found. Similar to the above classification, the bright localized excitations should lie in the gap below the bottom of the spin-wave spectrum, whereas their dark counterparts may occur at frequencies above the bottom spectrum edge.

By invoking the continuum approximation the same Eq. (6) is recovered for the slowly varying envelope $\psi_n = s_n$, but with different coefficients:

$$\alpha = \frac{\Omega(0) - \Omega}{\sqrt{1 + \frac{D^2}{4J^2}}}, \quad \beta = \frac{\Omega(0)}{2\sqrt{1 + \frac{D^2}{4J^2}}}. \tag{17}$$

Repeating the steps that led from Eq. (6) to DB modes, the previous solutions (8), (11) and (14) are recovered as breather lattices of the bright and dark types, respectively. However, there is a significant discrepancy in conditions for $\Omega$ and $B$ owing to the different definition for $\alpha$ and $\beta$. As expected, one gets $\Omega < \Omega(0)$ for the bright mode and $\Omega > \Omega(0)$ for the dark mode, which originates formally from the requirements $\alpha > 0$ or $\alpha < 0$, respectively. From a magnetic viewpoint, the emergence of these excitations is related to the restriction imposed on the constant of the single-ion anisotropy $B$. The bright modes ($\beta > 0$) appear at *easy-axis* anisotropy, $B < 1 - \sqrt{1 + D^2/4J^2}$, which automatically rules out excitations of this type for observation in $CrNb_3S_6$. The spatial distribution of magnetic moments of this type of DB mode, found numerically and corresponding to the model solution (11), is illustrated in Fig. 3. In addition to this, one may find a family of solutions (8) for the same set of parameters. In contrast, the dark modes ($\beta < 0$) comply with the opposite restriction $B > 1 - \sqrt{1 + D^2/4J^2}$, thereby admitting both fairly small easy-axis anisotropy ($B < 0$) and that of the easy-plane type ($B > 0$). Visualization of the spin arrangement for $B = 0.15$ is given in Fig. 4. It is precisely this type of DB excitations, which can be approximated by the *bottom dark* solution (14), that is relevant to the chiral helimagnet $CrNb_3S_6$.

## III. NUMERICAL SIMULATIONS OF DB MODES

When spin deviations of the breather modes grow to be large enough, the basic equation (6) of the theoretical treatment becomes invalid. This warrants additional numerical simulations to verify analytical results.

Our numerical procedure follows a scheme that has been suggested in Ref. [21]. Giving an initial guess for $s_1$, one can let $s_2$ be determined by the truncated version of Eq. (3):

$$\Omega s_1 = -2Bs_1\sqrt{1 - s_1^2} + s_1\sqrt{1 - s_2^2} - s_2\sqrt{1 - s_1^2}\sqrt{1 + q_0^2},$$

with $q_0^2 = \frac{D^2}{4J^2}$.

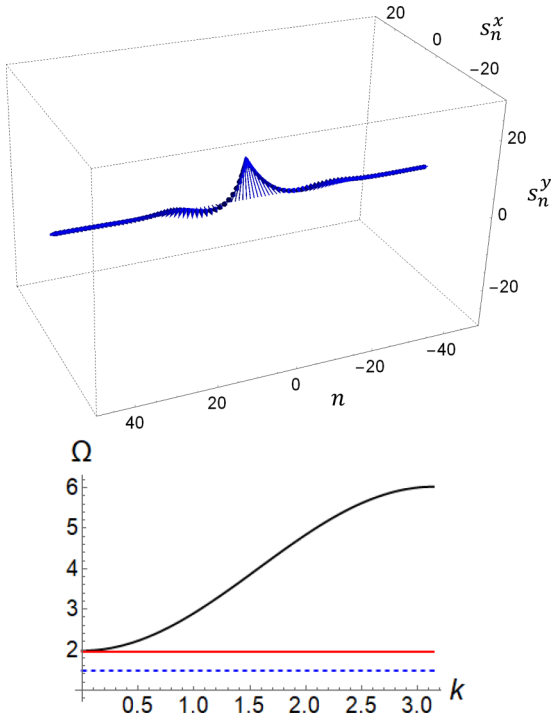


FIG. 3. The bottom bright breather mode with one kink-antikink bound pair in the envelope function built from numerical simulations (upper panel). Transversal spin components (relative to the chain axis) are shown with a factor 50 expansion. Lower panel: Dispersion curve $\Omega(k)$ for the linear spin-wave band (black solid) at the easy-axis anisotropy $B = -1.0$ (solid black). Frequency of the breather excitations $\Omega = 1.95$ (red solid) with the lowest boundary $\Omega_d = \frac{3}{2}[1 - B - \sqrt{1 + (D/2J)^2}]$ (blue dashed).

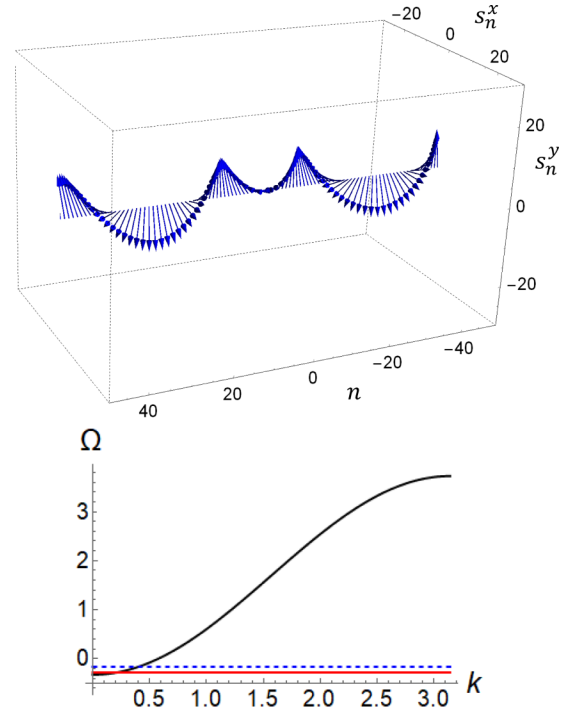


FIG. 4. The bottom dark breather mode with one kink in the envelope function built from numerical simulations (upper panel). Transversal spin components (relative to the chain axis) are shown with a factor 20 expansion. Lower panel: The spin-wave spectrum at the easy-plane anisotropy $B = 0.15$ (solid black). The breather frequency $\Omega = -0.28$ (red solid) is upper bounded by $\Omega_u = 1 - B - \sqrt{1 + (D/2J)^2}$ (blue dashed).

After the initialization steps the general recursion takes the form

$$s_{n+1} = \frac{-A_n\sqrt{(1 - s_n^2)(1 + q_0^2)} + \sqrt{1 + (1 - s_n^2)q_0^2 - A_n^2}}{1 + (1 - s_n^2)q_0^2}, \tag{18}$$

where

$$A_n = s_{n-1}\sqrt{1 - s_n^2}\sqrt{1 + q_0^2} + s_n\Big(\Omega - \sqrt{1 - s_{n-1}^2 + 2B\sqrt{1 - s_n^2}}\Big).$$

The node index $n$ runs through the lattice, until it eventually reaches the right end. The truncated equation for the right edge spins,

$$\Omega s_L = -s_{L-1}\sqrt{1 - s_L^2}\sqrt{1 + q_0^2} + s_L\sqrt{1 - s_{L-1}^2} - 2Bs_L\sqrt{1 - s_L^2}, \tag{19}$$

may be used as an inexpensive way to check the convergence of the iterative procedure. Solutions are generated by scanning $2 \times 10^{11}$ trial runs for $s_1$ from the range $[s_1, s_1 + h]$ with the step $h = 10^{-6}$.

Examples of the four DB types, which are determined by their frequency positions with respect to the spin-wave band, are illustrated in Figs. 1–4 (their temporal behavior may be seen in Figs. S1– S4 in Supplemental Material [61]). The chain length $L = 101$ and the constant DM strength $D/2J = 0.16$ have been taken in each case, only values for $\Omega$, $B$, and $s_1$ varied. In each of the plots, an additional line, bounding the possible frequency range of the breather excitations, is shown either inside or outside the spin-wave band. The boundary is established from the requirement that the amplitude of the appropriate single breather solution is limited to be less than 1. It can be easily seen from Eqs. (13) and (16) that this is equivalent to the conditions $2\alpha < \beta$ or $\beta < \alpha$ for bright or dark modes, respectively.

As such, only the bright breather modes may be associated with self-localized spin-wave excitations (or, *intrinsic localized modes*), where a scale of the localization may be on a scale comparable to the lattice spacing. In the case of the bottom bright breathers, the reason for this is that both the magnetic anisotropy and the magnetic field tend to align the moments all in the direction of the chain axis and only the DM interaction tries to prevent them. For the top bright breathers, the single-ion anisotropy acts already in alliance with the antisymmetric exchange coupling, but the interior antiferromagnetic order of moments restricts the spatial extent of these excitations.

The latter plays a key role in a difference between the dark breather solutions located at opposite ends of the spin-wave band. Although fairly small easy-plane anisotropy is permissible for both of them, there is an additional restriction on $B$

originating from the requirement that the frequency $\Omega$ of the interior spins must be the same as that of the end moments.

Indeed, the top dark breathers may arise at

$$\Omega > \Omega_d = 1 - B + \sqrt{1+q_0^2}. \tag{20}$$

On the other hand, Eq. (19) results in

$$\Omega \approx \sqrt{1-s_L^2}\left(1 - 2B + \sqrt{1+q_0^2}\right),$$

provided there is antiparallel alignment of the edge spins, $s_L \approx -s_{L-1}$. Then, as an immediate consequence,

$$\sqrt{1-s_L^2} > \frac{1 - B + \sqrt{1+q_0^2}}{1 - 2B + \sqrt{1+q_0^2}}, \tag{21}$$

which leads to the obvious contradiction $\sqrt{1-s_L^2} > 1$ for the easy-plane anisotropy $B > 0$.

The frequency of the bottom dark breathers is bounded above by $\Omega_u = 1 - B - \sqrt{1+q_0^2}$. Given the ferromagnetic arrangement of moments at the edge, $s_L \approx s_{L-1}$, we have from (19)

$$\Omega \approx \sqrt{1-s_L^2}\left(1 - 2B - \sqrt{1+q_0^2}\right).$$

Therefore

$$\sqrt{1-s_L^2} < \frac{B + \sqrt{1+q_0^2} - 1}{2B + \sqrt{1+q_0^2} - 1},$$

which amounts to the desired result $\sqrt{1-s_L^2} < 1$ for any positive $B$.

In the foregoing analysis it was tacitly assumed that the spatial arrangement of the spin variables $s_n$ is smooth in the vicinity of the edges and takes zero values only inside the chain. When, however, $s_L$ is small enough, the relationship $|s_L| \approx |s_{L-1}|$ is no longer applicable and dark breather solutions become possible only under a suitable choice of $B$, ensuring matching of a spin configuration scale to the chain length. That is the situation shown in Fig. 2. Moreover, solutions obtained thereby vary fairly rapidly with distance, which makes the continuum approximation ineffective for them.

We shall now turn to fitting the analytical expressions of Sec. II to the envelope function $\psi(z)$ obtained numerically to confirm the validity of the continuum approximation. Details of such a procedure for the top bright breather lattices have been discussed by us in Ref. [62]. The main purpose is to find the $c$ parameter and then deduce the elliptic modulus $\kappa$ from Eq. (9) with defined $\alpha$ and $\beta$. Note that in the case of the soliton lattice ground state, the constant $c$ is excluded from minimization of energy per unit length, since $c$ is related with the elliptic modulus $\kappa$. [63].

By definition, the constant $c$ arises as the first integral of Eq. (6):

$$c = \left(\frac{d\psi}{d\tilde{z}}\right)^2 - \alpha\psi^2 + \frac{\beta}{2}\psi^4. \tag{22}$$

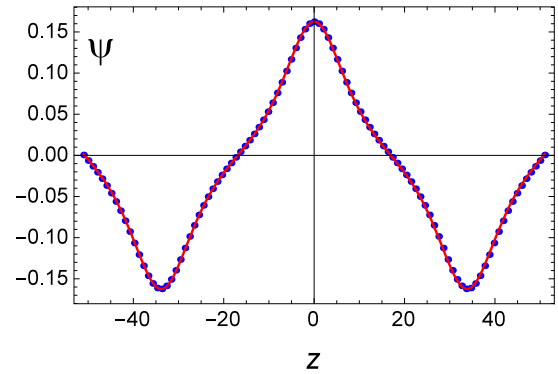


FIG. 5. The envelope function of the top bright breather lattice for $L = 101$ as predicted by Eq. (8). The solid red (dotted blue) line corresponds to analytical (numerical) calculation for $D/2J = 0.16$ with $B = 4.0$, $\Omega = -3.95$. The edge spin $s_{-L/2} = 0.000\,488\,23$.

On the other hand, the derivative of the envelope function at the chain edge is given by

$$\left(\frac{d\psi}{d\tilde{z}}\right)\Big|_{L/2} \approx \frac{1}{\sqrt{1+q_0^2}}\left(1 + \sqrt{1+q_0^2} - \Omega - 2B\right)\psi_{L/2} + \frac{1}{2\sqrt{1+q_0^2}}\left(2B - 1 - \sqrt{1+q_0^2}\right)\psi_{L/2}^3, \tag{23}$$

which directly follows from Eq. (3), if accounting for the open boundary conditions and neglecting nonlinear terms, including derivatives of the function $\psi$.

It can be envisaged that the envelope function is small at the edges of the chain due to intrinsic localization of the top bright breathers. Then Eqs. (22) and (23) result in the transcendental equation

$$c \approx \left(\alpha^2 + \alpha\frac{2 + \sqrt{1+q_0^2}}{\sqrt{1+q_0^2}} + 2\frac{1 + \sqrt{1+q_0^2}}{\sqrt{1+q_0^2}}\right)\psi_{L/2}^2.$$

Comparison of the envelope functions computed both numerically and analytically from Eq. (8) is presented in Fig. 5. Note that the top bright breather modes may be both on-site centered [64] and intersite centered [65]. This type of solution may be found below the spin-wave band as well (see Fig. 6), however, it requires the chain consisting of an even number of sites, since these modes are being intersite centered only. A comparing procedure between the numerical data and the model solution is similar to that of the dark BL modes, as explained below.

Figure 7 shows the numerical data superimposed on the analytical curve for the bottom bright breather, as given by Eq. (11). To render the fit with known $\alpha$ and $\beta$, it is convenient to make use the property of the solution, $\psi_{\min}/\psi_{\max} = \mathrm{dn}K = 1 - \kappa^2$, which yields $\kappa^2 \approx 0.994\,298$ in this case. Then the argument coefficient in the Jacobi nd-function is easily recovered as

$$\frac{1}{\sqrt{2}}\left(\alpha + \sqrt{\alpha^2 + 2\beta c}\right)^{\frac{1}{2}} = \sqrt{\frac{\alpha}{2-\kappa^2}} \approx 0.155\,293.$$

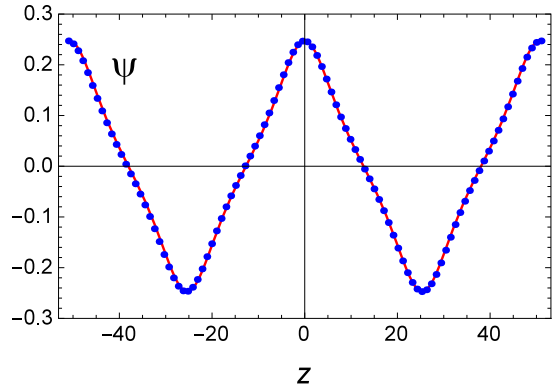


FIG. 6. The envelope function of the bottom bright breather lattice for $L = 100$ as predicted by Eq. (8). The solid red (dotted blue) line corresponds to analytical (numerical) calculation for $D/2J = 0.16$ with $B = -1.0$, $\Omega = 1.95$. The edge spin $s_{-L/2} = 0.247\,083\,08$.

It should be noted that although the top bright BL solutions (11) are admitted by the continuum theory, they are not reproduced numerically. This is probably related to antiparallel alignment of magnetic moments in these excitations.

Fitting for the dark BL solutions plotted in Figs. 8 and 9 follows the same template. At first one finds the constant

$$c = \psi_{\max}^2\left(|\alpha| - \frac{|\beta|}{2}\psi_{\max}^2\right),$$

where $\psi_{\max}$ is maximum value of the envelope function adopted from numerical data. Next the elliptic modulus (15) and the argument in the Jacobi sn-function (14) can be specified.

It is evident that predictions of the treatment based on the continuum approximation are in good agreement with their numerical counterparts. From now on, solutions requiring either easy-axis or strong easy-plane anisotropy are beyond the scope of our study, and we narrow focus on the bottom dark breathers only as the most likely candidate to be detected in $CrNb_3S_6$.

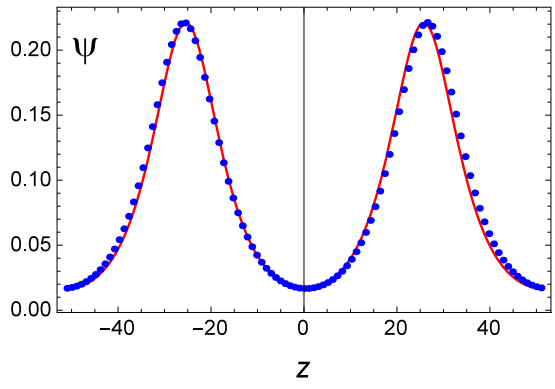


FIG. 7. The envelope function of the bottom bright breather lattice for $L = 101$ as predicted by Eq. (11). The solid red (dotted blue) line corresponds to analytical (numerical) calculation for $D/2J = 0.16$ with $B = -1.0$, $\Omega = 1.95$. The edge spin $s_{-L/2} = 0.016\,876\,628$.

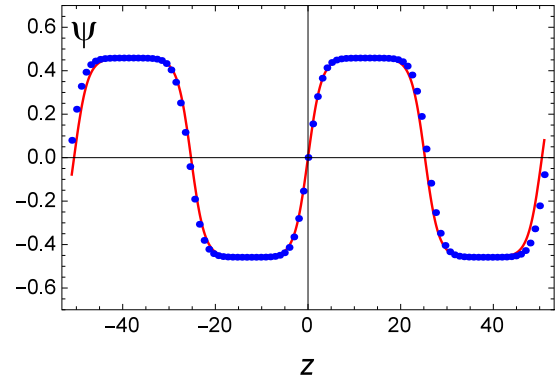


FIG. 8. The envelope function of the top dark breather lattice for $L = 101$ as predicted by Eq. (14). The solid red (dotted blue) line corresponds to analytical (numerical) calculation for $D/2J = 0.16$ with $B = 1.0$, $\Omega = 1.8$. The edge spin $s_{-L/2} = -0.079\,802\,639$.

## IV. BOTTOM DARK BREATHERS

To gain a deeper insight into the properties of the dark bottom breathers, we start off with their classification. Numerical simulations of these excitations for specific choices of the edge spin are depicted in Fig. 10. The main feature of the breather lattices is that their spatial period does not match the system size what resembles, in some respects, standing waves with soft pinning at boundaries [66,67]. Obviously, these solutions differ in a number $N$ of embedded kinks/antikinks, or, equivalently, by the number of nodes, which may be adopted as a criterion to categorize them. Finite spin deviations $s_{-L/2}$ needed to generate spin configurations of a given $N$ are slightly different from each other, but extremely high precision typical for top dark breather solutions is not required.

Next, we use the Floquet theory to examine the linear stability of the identified breather modes [23,68,69]. For the purpose, one has to study the evolution of a perturbation $\varepsilon_n(t)$ added to the DB periodic solution $s_n^{(0)}(t)$, i.e., $s_n(t) = s_n^{(0)}(t) + \varepsilon_n(t)$, for the lattice of $L$ sites with $n = 1, 2, \ldots, L$. Assuming that the size of perturbation is suitably small, one may linearize the resulting equations for $\varepsilon_n(t)$ deduced di-

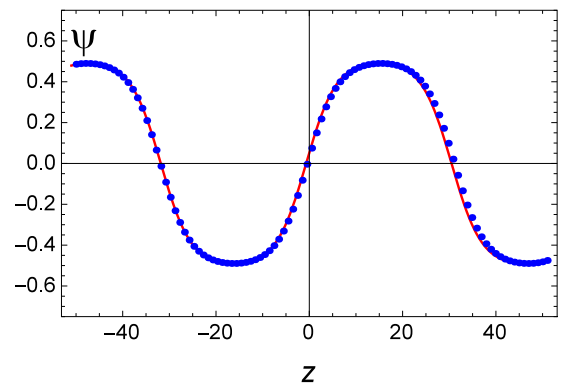


FIG. 9. The envelope function of the bottom dark breather lattice for $L = 101$ as predicted by Eq. (14). The solid red (dotted blue) line corresponds to analytical (numerical) calculation for $D/2J = 0.16$ with $B = 0.15$, $\Omega = -0.28$. The edge spin $s_{-L/2} = 0.485\,854\,468\,7$.

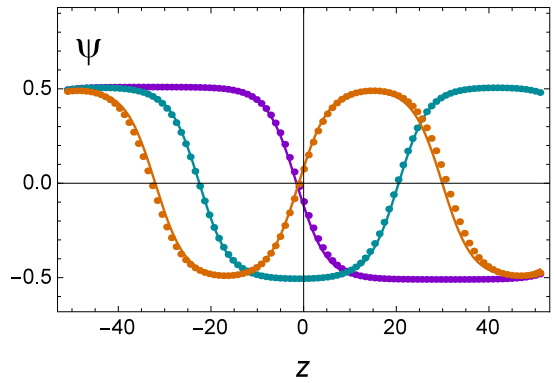


FIG. 10. The envelope function of the bottom dark breather lattice containing $N$ kinks: $N = 1$ (purple) with $s_{-L/2} = 0.495\,373$, $N = 2$ (teal) with $s_{-L/2} = 0.494\,843$, $N = 3$ (brown) with $s_{-L/2} = 0.485\,854$. The other parameters as in Fig. 9.

rectly from the equations of motion (2). Their explicit form looks rather cumbersome, but more importantly, the linearized system defines the monodromy matrix $\hat{M}$, which maps $s_n(t)$ into $s_n(t+T)$:

$$\begin{pmatrix} \varepsilon_n'(T) \\ \varepsilon_n''(T) \end{pmatrix} = \hat{\mathcal{M}} \begin{pmatrix} \varepsilon_n'(0) \\ \varepsilon_n''(0) \end{pmatrix}. \tag{24}$$

Here the period $T = \pi/\omega$ is only half the size of that of the periodic solutions $s_n^{(0)}(t)$. In addition, the complex nature of $\varepsilon_n$ has to be taken into account to separate it into the real $\varepsilon_n'$ and imaginary $\varepsilon_n''$ parts.

Any solution can be determined by the column matrix of the initial conditions $\Lambda(0) = [\varepsilon_1'(0), \varepsilon_1''(0), \ldots, \varepsilon_L'(0), \varepsilon_L''(0)]^T$. The monodromy matrix can be easily constructed numerically by integrating differential equations for $\varepsilon_n$ $2L$ times from $t = 0$ to $T$ with the initial conditions $\Lambda^\nu(0)$, $\nu = 1, 2, \ldots, 2L$, with the elements $\Lambda_\mu^\nu(0) = \delta_{\nu\mu}$. If the eigenvalues $\lambda$ of the monodromy matrix $\hat{\mathcal{M}}$ lie on the unit circle of the complex plane, then according to the Floquet theorem, the periodic orbit is stable, otherwise it is unstable.

Performing these calculations we obtain that the dark breather solutions are stable for any $\beta > \beta_{\rm cr} = 2\sqrt{1+q_0^2} + 2B - 1$ (hereinafter, $\beta = H/2JS$ is the magnetic field strength measured in the $2JS$ units). Close to the threshold point the Floquet eigenvalues are located almost uniformly on the unit circle, while far from $\beta_{\rm cr}$ they are redistributed being mostly concentrated on the left half of the unit circle, but stability is nonetheless retained (Fig. 11).

An interesting feature of the bottom dark breather solutions is their energy $E$ dependence on the number $N$ of embedded kinks. By rewriting the Hamiltonian (1) in terms of the spin variables $s_n$ we get the form

$$\frac{E}{2JS^2} = -\sqrt{1+q_0^2}\sum_{n=1}^{L-1} s_n s_{n+1} + B\sum_{n=1}^{L-1}\left(1 - s_n^2\right) - \sum_{n=1}^{L-1}\sqrt{1-s_n^2}\sqrt{1-s_{n+1}^2} - \beta\sum_{n=1}^{L-1}\sqrt{1-s_n^2}. \tag{25}$$

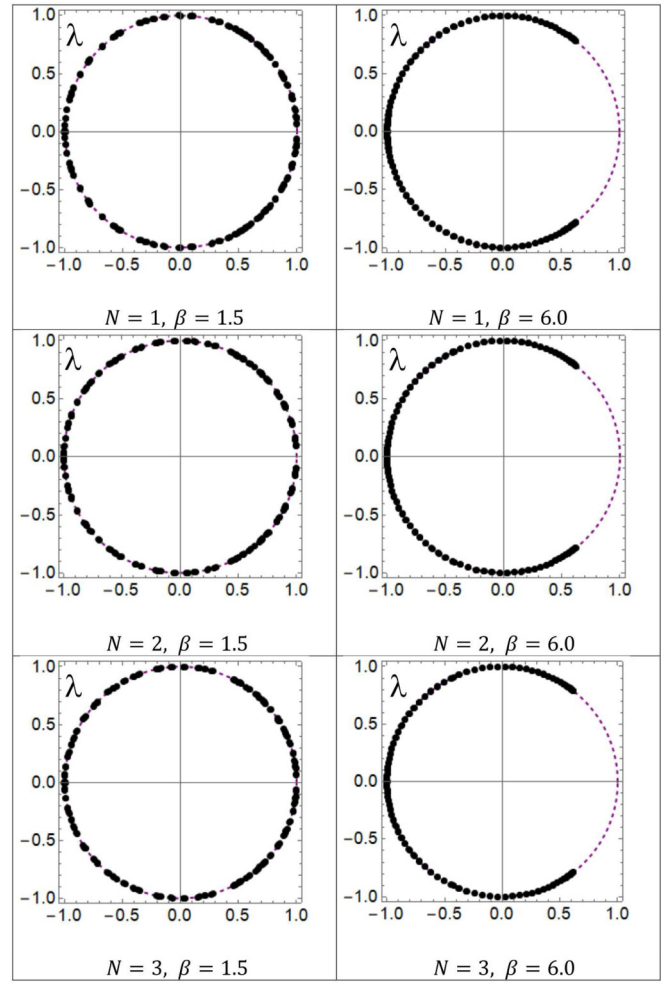


FIG. 11. Eigenvalues $\lambda$ of the monodromy matrix for the bottom dark breather lattices of size 101 with a different number of embedded kinks $N = 1, 2, 3$ in dependence on the magnetic field $\beta$. The parameters are $B = 0.15$, $\Omega = -0.28$, and $D/2J = 0.16$. The critical magnetic field $\beta_{\rm cr} = 1.325$.

With the help of the expression, the function $E_{\rm b}$, the energy per lattice bond measured from the ground-state value $E_0 = -1 + B - \beta$ is plotted against $N$ in Fig. 12 for different values of the frequency $\Omega$ with $B$ and $\beta$ fixed.

To understand this result recall that the orientation of the moments perpendicular to the chain axis is favorable from the viewpoint of easy-plane anisotropy; however, there is a significant increase in the Zeeman energy. With an addition of a kink/antikink the increase in the latter can be reduced in the vicinity of a kink center; however, this would give rise to an increase in the anisotropy energy. The competition of the two contributions, whereof the Zeeman term dominates since the ratio $B/\beta$ is on the order of 0.1, determines the details of dependence of $E_{\rm b}$ on $N$, which is projected on a straight line with negative slope (Fig. 12). The exchange interaction plays no role owing to its full rotational invariance and the almost parallel alignment of adjacent magnetic moments.

Being a continuous function of the frequency $\Omega$, the energy $E_b$ decreases gradually to zero when $\Omega$ varies from the upper boundary $\Omega_u = 1 - B - \sqrt{1+q_0^2}$ to the bottom edge

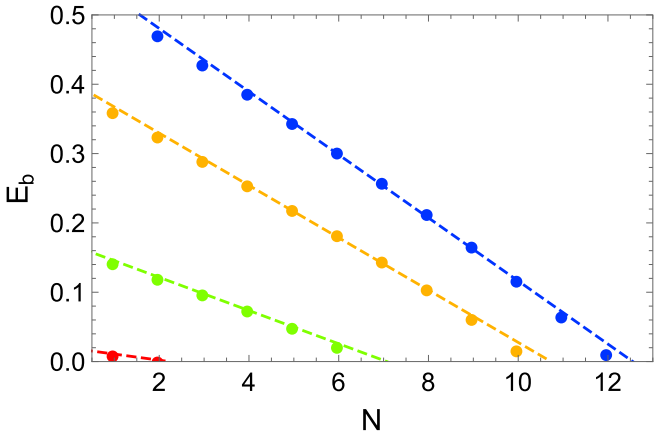


FIG. 12. Dependence of the BL energy per bond $E_b$ on the number of embedded kinks $N$ shown by dots for $\Omega = -0.18$ (blue), $\Omega = -0.22$ (brown), $\Omega = -0.28$ (green), and $\Omega = -0.32$ (red). Linear fitting to the numerical data is shown by the dashed lines. The parameters are $B = 0.15$, $D/2J = 0.16$, and $\beta = 1.5$. The frequencies are restricted to the range $\Omega(0) < \Omega < \Omega_u$ with $\Omega(0) = -0.325\,438$ and $\Omega_u = -0.162\,719$ (see the text) and corresponds to the physical frequencies $\omega$ as 1.485 THz ($\Omega = -0.18$), 1.440 THz ($\Omega = -0.22$), 1.373 THz ($\Omega = -0.28$), and 1.328 THz ($\Omega = -0.32$). The chain length $L = 101$.

of the spin-wave spectrum, $\Omega(0) = 2 - 2B - 2\sqrt{1+q_0^2}$. The requirement that $E_b$ should be non-negative imposes a restriction on a number of kinks in the breather lattice whereby the less breather frequency $\omega = 2JS(\Omega + \beta)/\hbar$, the less maximal number of kinks. It should be mentioned at this point that a similar trend has been experimentally observed in electrical lattices, where discrete breathers are produced via the well-known mechanism of modulation instability [70,71]. Numerical estimations for the physical frequency $\omega$ are given in Fig. 12 for $J = 18$ K and $S = 3/2$ relevant for $CrNb_3S_6$ [59]. Furthermore, according to our calculations, the amplitude of the breather lattice modes becomes larger for the modes of higher frequency but with the same number of kinks. By definition, it corresponds to the regime of hard nonlinearity.

Finally, we point out that each of the discrete BL solutions possesses the topological charge $\mathcal{Q} = \Delta\varphi/2\pi = kL_0^{(d)}/2\pi$, where $\Delta\varphi$ is the total angle of spin moment rotation around the $z$ axis per the BL period $L_d = 4K\sqrt{(1+\kappa^2)/|\alpha|}$. This quantity includes the wave vector $k = -a^{-1}\tan^{-1} q_0$ resulting from the DM interaction. The same factor appears in the expression for the linear momentum density $\mathcal{P}_n = \hbar k S(1 - \sqrt{1-s_n^2})$, which takes nonzero values whenever the transverse spin accumulation $s_n$ emerges. Thus the important consequences of the DM interaction are topological protection ensured by the topological charge and a possibility of sliding motion, which requires no expense of energy, provided by the nonzero linear momentum.

## V. RESULTS AND DISCUSSION

Noncollinear spin textures in chiral helimagnets and their concomitant fundamental excitations have aroused research interest as technologically relevant objects for spintronic applications [72–75]. Unfortunately, nonlinear breather excitations lie outside the mainstream of these investigations and the number of relevant works is very limited [76,77]. In our study we argue that this kind excitation may arise in the form of magnetic discrete breathers in the monoaxial chiral helimagnet $CrNb_3S_6$ owing to fairly small easy-plane anisotropy and the specific domain structure of the compound. The latter has strong impacts on standing spin waves in the thin films of $CrNb_3S_6$ [67]. Namely, the smallness of microdomains of definite crystallographic chirality necessitates a discrete approach to studying the breather modes.

We treat the phase of the forced ferromagnetic order, which is established above the threshold value of the external magnetic field directed along the chiral axis, and classify all types of possible solutions permitted by the model Hamiltonian of the monoaxial chiral helimagnet. Using the data on magnetic anisotropy in $CrNb_3S_6$, we estimate the relevance of these excitations and conclude that only the dark breather modes, having the form of the periodic breather lattice, are supported just above the bottom edge of the spin-wave spectrum. This kind of nonlinear solution, which is proved to be stable, supplements the diversity of nontrivial spin structures in chiral helimagnets and may contribute to the spin response in electron spin resonance experiments.

The proposed classification scheme of DB solutions within the continuum approach offers a natural interpretation of findings of the early numerical studies on intrinsic localized spin modes in ferromagnetic Heisenberg chains [21,52]. It should be pointed out, however, that the inclusion of the Dzyaloshinskii-Moriya interaction is not simply a consideration for an additional form of magnetic anisotropy; the antisymmetric exchange provides topological charge and linear momentum for emerging breather modes.

In accordance with a generally accepted concept, DB modes owe their existence to two pivotal components—discreteness and nonlinearity. In the case of $CrNb_3S_6$, the discrete nature becomes evident by comparing the characteristic domain size $L \sim 1$ $\mu$m with the BL period $L_0$. Our calculations show (see, for instance, Fig. 10) that the period encompasses around 100 sites that yield $L_0 \sim 0.1$ $\mu$m, i.e., only one-tenth of $L$, if the distance 6.847 Åbetween the nearest Cr ions along the chiral axis [78] is accounted for. The nonlinearity of our problem is guaranteed by the single-ion anisotropy $B$ and the constraint that the spin length is conserved in dynamical processes.

The dark breather lattices may be classified by the number $N$ of embedded kinks/antikinks, but modes with the same $N$ may appear at different frequencies going by the rule whereby the higher the frequency, the bigger the amplitude. This fact imposes severe restrictions upon a maximum value of kinks/antikinks that can be accommodated in a finite-length segment. A striking feature of the dark breather lattice is its energy, which decreases linearly with increasing $N$, in contrast to linear growth for bright modes [62]. This strange behavior reflects a competition in the phase of forced ferromagnetism between the single-ion anisotropy, the antisymmetric exchange, and the Zeeman coupling, whereof the last interaction dominates and which specifically makes the phase stable.

These findings mean that the micron-sized domain of $CrNb_3S_6$, in which the DB lattice is excited, is a system

where areas of stored energy are linked to regions of transverse spin accumulation. As such, there arises a strictly 1D periodic array of resonators whose stored energy can take only discrete values and is controlled by two degrees of freedom, namely, the kink/antikink number $N$ (or equivalently, by the BL period) and the BL frequency $\omega$ (or equivalently, by the BL amplitude). According to our order-of-magnitude estimate, $\omega$ lies in the terahertz range. Because of nonlinearity, an amount of stored energy in these "breather capacitors" will be far beyond the capacity of standing spin waves. This functionality may be used to design spintronic resonators on the base of chiral helimagnets. Care should be taken to exclude resonances with linear spin waves, since frequencies of the dark breather modes lie inside the SW band. While the discreteness of the system ensures that these resonances may be avoided if the breather mode frequency is appropriately chosen, this issue requires more detailed examination in the framework of the special theory [79,80]. Another open issue relates to a way to excite in a controllable manner these breather modes by external sources. The creation of special microfabricated microwave antennae, like those used in a noncentrosymmetrical ferromagnet $LiFe_5O_8$ to induce magnons with large momentum, appears to be a promising way [81]. In this case, the microwave wavelength emitted by the antenna must be matched with a period of the excited BL mode. These challenges posed by the practical application together with the basic problem of finding similar discrete breather modes in the other ordered phases of the monoaxial chiral helimagnet, i.e., the conical and soliton lattice phases, should be addressed in future works.

## VI. CONCLUSIONS

In summary, we investigate the possibility of experimental observation of discrete breather excitations in the forced ferromagnetic phase of the monoaxial chiral helimagnet $CrNb_3S_6$. We found that the presence of the DM interaction does not prevent their emergence but, conversely, ensures their topological protection. We demonstrate that the model Hamiltonian of the monoaxial chiral helimagnet supports several kinds of possible spatially periodic discrete breather solutions, but a specific choice depends on subtle interplay between interactions accounted for in the Hamiltonian. Using experimental data for strengths of the DM coupling and the easy-plane single-ion anisotropy in $CrNb_3S_6$, we predict for this magnetic material the appearance of the dark breather lattice modes with frequencies lying within the linear spin-wave spectrum near to its bottom edge. Results of numerical simulations of the DB excitations on a finite-length chain are in very good agreement with the continuum approximation, which relates the DB lattice modes and periodic solutions of the nonlinear Duffing equation. The Floquet analysis confirms the stability of the discrete breather excitations relevant for $CrNb_3S_6$. Their classification, based on a number of embedded kinks/antikinks, is suggested, and the dependence of their energy inversely proportional to this number is established. This unusual feature of the dark breather lattice modes positioned just above the spin-wave band bottom paves a way to design spintronic capacitors based on chiral helimagnets and operates on the principle energy pumping from the DB modes to the magnon sector.

## ACKNOWLEDGMENTS

This work was supported by the Act of the Government of the Russian Federation (Contract No. 02.A03.21.0006). I.G.B., E.G.E., and V.E.S. acknowledge financial support by the Russian Foundation for Basic Research (RFBR), Grant No. 20-02-00213. A.S.O. thanks the Russian Foundation for Basic Research (RFBR), Grant No. 20-52-50005, and the Ministry of Science and Higher Education of the Russian Federation, Project No. FEUZ-2020-0054. J.K. acknowledges financial support by JSPS KAKENHI Grant No. 17H02923.

## APPENDIX: DUFFING EQUATION

In the long wave limit, when a characteristic spatial scale of DB solutions is much larger than the lattice unit $a$, one may proceed with the continuous coordinate $z = na$ instead of the discrete parameter $n$ in Eq. (3).

Approximating the spin variables by their continuous counterparts,

$$s_n = (-1)^n \psi(z), \tag{A1}$$

$$s_{n\pm1} = (-1)^{n\pm1}\left[\psi(z) \pm a\frac{d\psi}{dz} + \frac{a^2}{2}\frac{d^2\psi}{dz^2}\right], \tag{A2}$$

$$\sqrt{1-s_n^2} \approx 1 - \frac{1}{2}\psi^2(z), \tag{A3}$$

$$\sqrt{1-s_{n\pm1}^2} \approx 1 - \frac{1}{2}\psi^2(z) \mp a\psi(z)\frac{d\psi(z)}{dz}, \tag{A4}$$

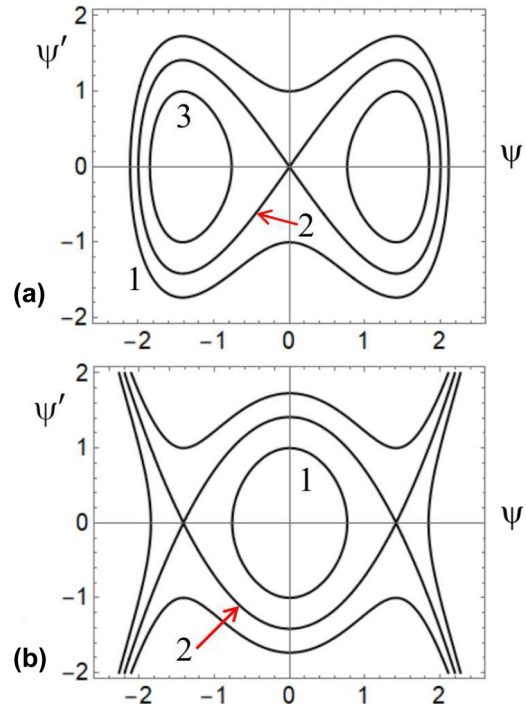


FIG. 13. Phase portraits of the Duffing equation (6). (a) The bright solutions at $\alpha = 2$ and $\beta = 1$; (b) the dark solutions at $\alpha = -2$ and $\beta = -1$.

and substituting them into Eq. (3), we obtain eventually the classical Duffing equation (6) if nonlinear terms involving $d\psi/dz$ and $d^2\psi/dz^2$ are neglected.

The behavior of restricted solutions of the Duffing equation (6) is clearly illustrated by their trajectories on the phase plane $(\psi, d\psi/dz)$. A type of the solution depends on the signs of the coefficients $\alpha$ and $\beta$ (see, for example, Ref. [82]).

If $\alpha > 0$, $\beta > 0$ [Fig. 13(a)], the phase trajectories 1, 2, and 3 conform with the breather solutions (8), (13), and (11), respectively. This is the case of the bright modes.

If $\alpha < 0$, $\beta < 0$ [Fig. 13(b)], the phase trajectories 1 and 2 correspond to (14) and (16), respectively. This is the case of the dark modes.


[1] A. M. Kosevich, B. A. Ivanov, and A. S. Kovalev, Phys. Rep. **194**, 117 (1990).
[2] E. Infeld and G. Rowlands, *Nonlinear Waves, Solitons and Chaos* (Cambridge University Press, Cambridge, 1990).
[3] S. Flach and C. R. Willis, Phys. Rep. **295**, 181 (1998).
[4] S. Flach and A. V. Gorbach, Phys. Rep. **467**, 1 (2008).
[5] S. V. Dmitriev, E. A. Korznikova, Yu. A. Baimova, and M. G. Velarde, Phys. Usp. **59**, 446 (2016).
[6] S. R. Bickham, S. A. Kiselev, and A. J. Sievers, in *Spectroscopy and Dynamics of Collective Excitations in Solids, NATO ASI Series B* (Springer, Boston, MA, 1997), Vol. 356, p. 417.
[7] B. I. Swanson, J. A. Brozik, S. P. Love, G. F. Strouse, A. P. Shreve, A. R. Bishop, W.-Z. Wang, and M. I. Salkola, Phys. Rev. Lett. **82**, 3288 (1999).
[8] M. E. Manley, O. Hellman, N. Shulumba, A. F. May, P. J. Stonaha, J. W. Lynn, V. O. Garlea, A. Alatas, R. P. Hermann, J. D. Budai, H. Wang, B. C. Sales, and A. J. Minnich, Nat. Commun. **10**, 1928 (2019).
[9] F. M. Russell and J. C. Eilbeck, Europhys. Lett. **78**, 10004 (2007).
[10] P. Binder, D. Abraimov, A. V. Ustinov, S. Flach, and Y. Zolotaryuk, Phys. Rev. Lett. **84**, 745 (2000).
[11] E. Trías, J. J. Mazo, and T. P. Orlando, Phys. Rev. Lett. **84**, 741 (2000).
[12] J. Cuevas, L. Q. English, P. G. Kevrekidis, and M. Anderson, Phys. Rev. Lett. **102**, 224101 (2009).
[13] M. Sato, B. E. Hubbard, L. Q. English, A. J. Sievers, B. Ilic, D. A. Czaplewski, and H. G. Craighead, Chaos **13**, 702 (2003).
[14] H. S. Eisenberg, Y. Silberberg, R. Morandotti, A. R. Boyd, and J. S. Aitchison, Phys. Rev. Lett. **81**, 3383 (1998).
[15] N. Boechler, G. Theocharis, S. Job, P. G. Kevrekidis, Mason A. Porter, and C. Daraio, Phys. Rev. Lett. **104**, 244302 (2010).
[16] K. Narahara, J. Phys. Soc. Jpn. **89**, 074005 (2020).
[17] R. Lai and A. J. Sievers, Phys. Rep. **314**, 147 (1999).
[18] U. T. Schwarz, L. Q. English, and A. J. Sievers, Phys. Rev. Lett. **83**, 223 (1999).
[19] M. Sato and A. J. Sievers, Nature (London) **432**, 486 (2004).
[20] R. F. Wallis, D. L. Mills, and A. D. Boardman, Phys. Rev. B **52**, R3828 (1995).
[21] S. Rakhmanova and D. L. Mills, Phys. Rev. B **54**, 9225 (1996).
[22] Y. Zolotaryuk, S. Flach, and V. Fleurov, Phys. Rev. B **63**, 214422 (2001).
[23] J. M. Khalack, Y. Zolotaryuk, and P. L. Christiansen, Chaos **13**, 683 (2003).
[24] M. Lakshmanan, B. Subash, and A. Saxena, Phys. Lett. A **378**, 1119 (2014).
[25] M. Lakshmanan and A. Saxena, Phys. Lett. A **382**, 1890 (2018).
[26] R. S. Kamburova, S. K. Varbev, and M. T. Primatarowa, Phys. Lett. A **383**, 471 (2019).
[27] Z. I. Djoufack, E. Tala-Tebue, J. P. Nguenang, and A. Kenfack-Jiotsa, Chaos **26**, 103110 (2016).
[28] L. Kavitha, E. Parasuraman, D. Gopi, A. Prabhu, and R. A. Vicencio, J. Magn. Magn. Mater. **401**, 394 (2016).
[29] R. L. Pylypchuk and Y. Zolotaryuk, Low Temp. Phys. **41**, 733 (2015).
[30] A. M. Kosevich and A. S. Kovalev, Sov. Phys. JETP **67**, 1793 (1974).
[31] B. A. Ivanov, A. M. Kosevich, and I. M. Babich, JETP Lett. **29**, 777 (1979).
[32] V. G. Baryakhtar, M. V. Chetkin, B. A. Ivanov, and S. N. Gadetskii, *Dynamics of Topological Magnetic Solitons: Experiment and Theory (Springer Tracts in Modern Physics)* (Springer, New York, 1994).
[33] N. Papanicolaou, Phys. Rev. B **55**, 12290 (1997).
[34] A. V. Gorbach and S. Flach, Phys. Rev. E **72**, 056607 (2005).
[35] X. Quan and T. Qiang, Commun. Theor. Phys. **51**, 153 (2009).
[36] P. F. Byrd and M. D. Friedman, *Handbook of Elliptic Integrals for Engineers and Physics* (Springer-Verlag, Berlin, 1954).
[37] R. McLachlan, Math. Intelligencer **16**, 31 (1994).
[38] P. G. Kevrekidis, A. Saxena, and A. R. Bishop, Phys. Rev. E **64**, 026613 (2001).
[39] Z. Fu, S. Liu, and S. Liu, Phys. Scr. **76**, 15 (2007).
[40] Z. Fu and S. Liu, Z. Naturforsch. **62a**, 555 (2007).
[41] P. G. Kevrekidis, A. Khare, and A. Saxena, Phys. Rev. E **68**, 047701 (2003).
[42] P. G. Kevrekidis, A. Khare, A. Saxena, and G. Herring, J. Phys. A: Math. Gen. **37**, 10959 (2004).
[43] Z. Yan, Phys. Lett. A **372**, 969 (2008).
[44] X. Zhao, Z. T. Fu, J. Y. Mao, and S. K. Liu, Commun. Theor. Phys. **52**, 23 (2009).
[45] Z. Fu, S. Liu, and S. Liu, Phys. Lett. A **368**, 238 (2007).
[46] A. P. Tankeyev, V. V. Smagin, M. A. Borich, and A. S. Zhuravlev, Phys. Met. Metallogr. **107**, 229 (2009).
[47] A. P. Tankeyev, M. A. Borich, and V. V. Smagin, Phys. Met. Metallogr. **110**, 689 (2010).
[48] V. V. Smagin, A. P. Tankeyev, and M. A. Borich, Phys. Met. Metallogr. **108**, 425 (2009).
[49] F. Yin and B. Tang, Int. J. Theor. Phys. **57**, 2843 (2018).
[50] X. Quan and T. Qiang, Chin. Phys. Lett. **25**, 2400 (2008).
[51] R. I. Babicheva, A. S. Semenov, E. G. Soboleva, A. A. Kudreyko, K. Zhou, and S. V. Dmitriev, Phys. Rev. E **103**, 052202 (2021).
[52] S. V. Rakhmanova and A. V. Shchegrov, Phys. Rev. B **57**, R14012 (1998).
[53] A. M. Weiner, J. P. Heritage, R. J. Hawkins, R. N. Thurston, E. M. Kirschner, D. E. Leaird, and W. J. Tomlinson, Phys. Rev. Lett. **61**, 2445 (1988).

[54] C. Bao, Y. Xuan, C. Wang, A. Fülöp, D. E. Leaird, V. Torres-Company, M. Qi, and A. M. Weiner, Phys. Rev. Lett. **121**, 257401 (2018).
[55] Y. Togawa, T. Koyama, Y. Nishimori, Y. Matsumoto, S. McVitie, D. McGrouther, R. L. Stamps, Y. Kousaka, J. Akimitsu, S. Nishihara, K. Inoue, I. G. Bostrem, Vl. E. Sinitsyn, A. S. Ovchinnikov, and J. Kishine, Phys. Rev. B **92**, 220412(R) (2015).
[56] B. Schmid, B. Dorner, D. Petitgrand, L. P. Regnault, and M. Steiner, Z. Phys. B **95**, 13 (1994).
[57] J. Kishine and A. S. Ovchinnikov, in *Theory of Monoaxial Chiral Helimagnet*, edited by R. E. Campley and R. L. Stamps, Solid State Physics Vol. 66 (Academic Press, New York, 2015).
[58] T. Miyadai, K. Kikuchi, H. Kondo, S. Sakka, M. Arai, and Y. Ishikawa, J. Phys. Soc. Jpn. **52**, 1394 (1983).
[59] M. Shinozaki, S. Hoshino, Y. Masaki, J. Kishine, and Y. Kato, J. Phys. Soc. Jpn. **85**, 074710 (2016).
[60] A. A. Anders, G. V. Borisenko, and S. V. Volotskii, Sov. J. Low Temp. Phys. **15**, 21 (1989).
[61] See Supplemental Material at http://link.aps.org/supplemental/10.1103/PhysRevB.104.214420 for temporal oscillations of the discrete breather lattice solutions.
[62] I. G. Bostrem, Vl. E. Sinitsyn, A. S. Ovchinnikov, E. G. Ekomasov, and J. Kishine, AIP Adv. **11**, 015208 (2021).
[63] I. E. Dzyaloshinskii, Sov. Phys. JETP **19**, 960 (1964); **20**, 665 (1965).
[64] A. J. Sievers and S. Takeno, Phys. Rev. Lett. **61**, 970 (1988).
[65] J. B. Page, Phys. Rev. B **41**, 7835 (1990).
[66] P. Pincus, Phys. Rev. **118**, 658 (1960).
[67] J. Kishine, Vl. E. Sinitsyn, I. G. Bostrem, Igor Proskurin, F. J. T. Goncalves, Y. Togawa, and A. S. Ovchinnikov, Phys. Rev. B **100**, 024411 (2019).
[68] J. L. Marín, S. Aubry, and L. M. Floría, Physica D **113**, 283 (1998).
[69] J. F. R. Archilla, J. Cuevas, B. Sánchez-Rey, and A. Alvarez, Physica D **180**, 235 (2003).
[70] L. Q. English, F. Palmero, A. J. Sievers, P. G. Kevrekidis, and D. H. Barnak, Phys. Rev. E **81**, 046605 (2010).
[71] F. Palmero, L. Q. English, J. Cuevas, R. Carretero-González, and P. G. Kevrekidis, Phys. Rev. E **84**, 026605 (2011).
[72] B. Göbel, I. Mertig, and O. A. Tretyakov, Phys. Rep. **895**, 1 (2021).
[73] K. Inoue, Chem. Lett. **50**, 742 (2021).
[74] S.-H. Yang, Appl. Phys. Lett. **116**, 120502 (2020).
[75] C. Zhang, J. Zhang, C. Liu, S. Zhang, Y. Yuan, P. Li, Y. Wen, Z. Jiang, B. Zhou, Y. Lei, D. Zheng, C. Song, Z. Hou, W. Mi, U. Schwingenschlögl, A. Manchon, Z. Q. Qiu, H. N. Alshareef, Y. Peng, and X.-X. Zhang, Adv. Mater. **33**, 2101131 (2021).
[76] V. V. Kiselev and A. A. Raskovalov, Theor. Math. Phys. **173**, 1565 (2012).
[77] V. V. Kiselev and A. A. Raskovalov, J. Exp. Theor. Phys. **116**, 272 (2013).
[78] N. J. Ghimire, M. A. McGuire, D. S. Parker, B. Sipos, S. Tang, J.-Q. Yan, B. C. Sales, and D. Mandrus, Phys. Rev. B **87**, 104403 (2013).
[79] G. Kopidakis and S. Aubry, Physica D **130**, 155 (1999).
[80] G. Kopidakis and S. Aubry, Phys. Rev. Lett. **84**, 3236 (2000).
[81] Y. Iguchi, S. Uemura, K. Ueno, and Y. Onose, Phys. Rev. B **92**, 184419 (2015).
[82] L. A. Ostrovsky and A. I. Potapov, *Modulated Waves Theory and Application* (Johns Hopkins University Press, Baltimore, MD, 2002).

*Correction:* The first initial of the last author contained an error and has been set right.